Unusual spin-orbit control in AlInAs/GaInAs triple wells triggered by band crossing and anticrossing

Wen Liu,[1,2,*] Hao Yang,[1,*] and Jiyong Fu[1,3,†]
[1]*Department of Physics, Qufu Normal University, 273165 Qufu, Shandong, China*
[2]*Department of Physics, Jining University, 273155 Qufu, Shandong, China*
[3]*Instituto de Física, Universidade de Brasília, Brasília-DF 70919-970, Brazil*

(Received 28 February 2021; revised 26 July 2021; accepted 15 October 2021; published 29 October 2021)

Additional orbital degrees of freedom in multiband quantum systems may offer more intriguing possibilities for spin-orbit (SO) control. Here we explore the Rashba and Dresselhaus SO couplings in realistic AlInAs/GaInAs triple wells subjected to top (V_T) and back (V_B) gate potentials, allowing for flexible triple-occupancy control for electrons. By performing a self-consistent Poisson-Schrödinger calculation, we determine all the relevant Rashba (Dresselhaus) SO terms of both intraband α_ν (β_ν) and interband $\eta_{\mu\nu}$ ($\Gamma_{\mu\nu}$) types. For a structurally symmetric triple well, we achieve a *crossing* of energy levels between the first and second subbands and sequentially an *anticrossing* between the second and third subbands, accompanied with a double band swapping, simply *via* adjusting V_B. As a consequence, when V_B varies, an emerging interchange of the first-subband α_1 (β_1) and second-subband α_2 (β_2) SO terms, and of α_2 (β_2) and α_3 (β_3) respectively for the second and third subbands, i.e., double SO interchange, occurs, greatly fascinating for selective SO control among distinct subbands in spintronic devices. Further, near the two-band swapping points, across which electron transfer among the three local wells (triple well) takes place, detailed interchanging features of nonlinear SO control are also contrasting. Remarkably, in addition to Rashba terms, we also realize a wide-range control of Dresselhaus couplings, which are usually immune to electrical manipulation. Regarding the interband Rashba and Dresselhaus SO contributions, $\eta_{\mu\nu}$ and $\Gamma_{\mu\nu}$ exhibit either a *resonant* behavior or a *steplike* jump across band-swapping points, depending on the parity and spatial distribution of electron wave functions. By varying the barrier height of the two inner barriers in the triple-well configuration, dependence of relevant SO terms on engineered structures, which are either structurally symmetric or asymmetric, is also discussed. Interestingly, in the latter asymmetric case, we realize a *seemingly* symmetric configuration by adjusting V_B, in which α_1 and α_2 essentially vanish while α_3 is nonzero, providing a handle for suppressing electron spin relaxation of chosen subbands. Our results will stimulate more experiments probing unusual SO features in multiband and multiwell quantum systems and act as a guide for more proposals designed for spintronic devices.

DOI: 10.1103/PhysRevB.104.165428

I. INTRODUCTION

Control of spin is a prerequisite from fundamental physics to quantum information technology and spintronic devices [1,2]. The spin-orbit (SO) interaction couples electron spin and momentum via an effective magnetic field, facilitating coherent spin manipulation [3]. In 2D materials of transition metal dichalcogenides, the SO coupling acts as a central ingredient giving rise to the intriguing property of spin-valley *locking* [4–6]. Further, SO coupling can be essential for several intriguing quantum states, e.g., topological insulators [7], Majorana fermions [8,9], and Weyl semimetals [10]. Our recent proposals of persistent skyrmion lattice [11], stretchable spin helix [12], spin-helix symmetry breaking [13], and opposite SO control [14] also indicate the important role of SO effects in semiconductor spintronic applications.

Semiconductors such as GaAs, InAs, and InSb offer various strengths of SO couplings [12,15–18], and are thus suitable for a broad range of spintronic applications, making this subject extraordinarily profound. Very recently, we also explored in detail SO properties of wide-gap (e.g., GaN) semiconductors in the wurtzite phase, and obtained a general effective Hamiltonian for electrons valid for quantum wells, wires, and even dots [19]; Kammermeier *et al.*, demonstrated persistent spin textures and currents in SO-coupled wurtzite nanowire-based quantum structures [20], further extending this field.

In semiconductor nanostructures, the SO effects usually have two dominant contributions: the Rashba [21] and Dresselhaus [22] terms, arising from the breaking of the structural and crystal inversion symmetries, respectively. The Rashba coefficient can be tuned with the doping profile or by using an external bias [16,23]. In contrast, the Dresselhaus SO term mainly depends on quantum confinement [24,25]. The SO interaction was usually studied in semiconductor quantum wells with electrons only occupying the first subband ("single occupancy"), including the control of spin relaxation anisotropy [26–28], persistent spin helix [24,29–32], and quantum geometry associated SO features [25,33,34]. In addition, quantum wells with two populated subbands ("double occupancy") have also drawn growing interest due to emerging novel SO features arising from an additional orbital degree of freedom

*These authors contributed equally to this work.
†yongjf@qfnu.edu.cn

 ©2021 American Physical Society

[18,35–39], such as unusual spin textures [37,40], intrinsic spin-Hall effect [38], and crossed spin helices [11], as well as the associated spin dynamics of diffusion and drift [41–43].

Recently, triple-well structures with three occupied subbands, which are important in diverse fields of physics, e.g., quantum interference [44], Kerr nonlinearity [45], and optical bistability and multistability [46], have also been attracting intense attention in the field of spintronics. This is mainly because (i) a triple-well configuration favors flexible control of triple occupancy for electrons, (ii) additional orbital degrees of freedom may offer more intriguing SO features, and (iii) charge transfer among the three (left, central, and right) local wells provides more possibility for spintronic applications. For instance, Ullah *et al.* revealed strong anisotropy of spin relaxation time and long spin transport length (exceeding a half millimeter) in GaAs triple wells [47–49]; Wiedmann *et al.* demonstrated peculiar magnetointersubband oscillations [50] and Santos *et al.* observed quantum-Hall gap collapses [51] in the magnetoresistance measurements. Further, Cruiz and Luiz proposed an efficient spin-filter device in a triple-well system, where the injected electronic current that is initially unpolarized could be divided into two spin-up and spin-down polarized currents [52]. Also, very recently, Iijima and Akera demonstrated gate-induced switching of the spin-relaxation rate in a triple-well structure, achieving an efficient on:off ratio of the current in spin-field-effect transistor [53]. However, despite substantial efforts, detailed SO features in quantum systems with flexible tuning of the electron occupancy of three subbands, which may have more profound applications in future spintronic devices, still remain obscure.

Here we aim to unveil Rashba and Dresselhaus SO features of both intra- and interband types in triple wells, allowing for flexible control of triple occupancy for electrons. We consider realistic *n*-type AlInAs/GaInAs triple wells, which have relatively strong SO strength (cf. GaAs) [33,54,55], formed by embedding two inner barriers of heights δ_2 and δ_2' and subjected to top (V_T) and back (V_B) gate potentials [Figs. 1(a) and 1(b)]. By performing a self-consistent Poisson-Schrödinger calculation in the Hartree approximation, we determine all the relevant Rashba (Dresselhaus) SO terms of both intraband α_ν (β_ν) and interband $\eta_{\mu\nu}$ ($\Gamma_{\mu\nu}$) kinds.

Interestingly, for a structurally symmetric well, we achieve a band crossing and sequentially a band anticrossing, with the former for the first and second subbands and the latter for the second and third subbands, simply *via* adjusting V_B [Fig. 1(d)], indicating the emergence of double band swapping. We find that the band swappings are accompanied by spatial redistributions among the three (left, central, and right) local wells, which constitute the triple-well configuration, for electrons occupying the three subbands (Fig. 2). This follows an intriguing interchange of the first-subband α_1 (β_1) and second-subband α_2 (β_2) SO terms, and sequentially of α_2 (β_2) and α_3 (β_3) respectively for the second and third subbands, i.e., double SO interchange [Figs. 1(e) and 1(f)], greatly fascinating for selective SO control among distinct subbands in spintronic devices. Further, even near the two band-swapping points, detailed interchanging features of nonlinear SO control are also contrasting, because of distinct coupling strengths between involved subbands determining the band crossing or anticrossing. Remarkably, in addition to Rashba terms, we also realize a wide-range control of Dresselhaus couplings, which are usually immune to electrical manipulation, ensuring triple-wells ideal candidates for a simultaneous control of Rashba and Dresselhaus SO couplings *via* electrical means. Regarding the interband Rashba and Dresselhaus SO contributions, $\eta_{\mu\nu}$ and $\Gamma_{\mu\nu}$ exhibit either a *resonant* behavior or a *steplike* jump across the band-swapping points (Fig. 3), depending on the parity and spatial distribution of electron wave functions.

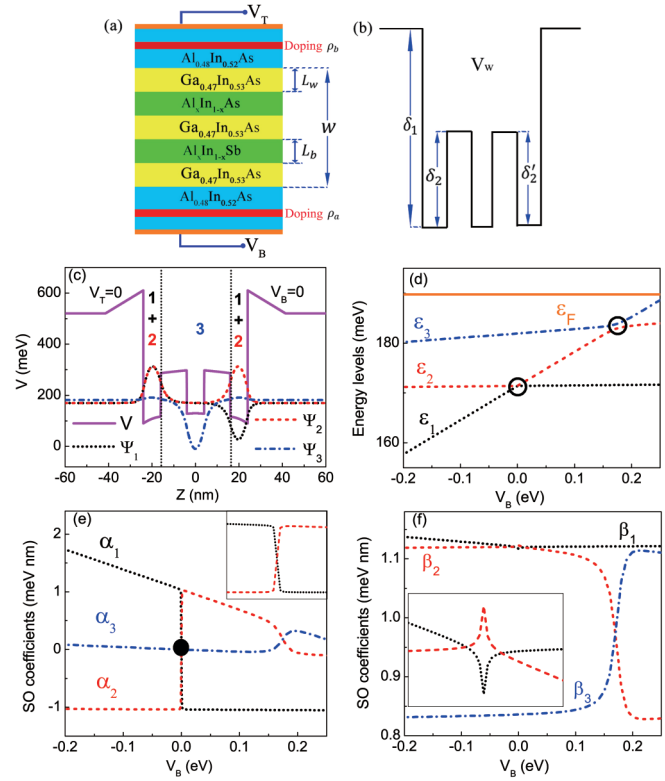

FIG. 1. (a) Schematic diagram of AlInAs/GaInAs triple well, with w, L_w, and L_b denoting the width of the overall well, three local wells ($Ga_{0.47}In_{0.53}As$), and embedded inner barriers ($Al_xIn_{1-x}As$), respectively. The red regions inside the outer barriers ($Al_{0.48}In_{0.52}As$) stand for doping layers with the doping density ρ_a and ρ_b. Top (V_T) and back (V_B) gate potentials are adopted to adjust the well symmetry and electron occupancy. (b) Schematic of the structural potential (V_w) of the triple well in (a), where δ_1 and δ_2 (δ_2') denote the outer and left (right) inner band offsets, respectively. (c) Zero-bias self-consistent potential V and wave function profiles ψ_ν ($\nu = 1, 2, 3$) of a symmetric triple well with $\delta_2 = \delta_2' = 0.17$ eV. The label "1+2" indicates that electrons in the left and right local wells are predominantly in states of both ψ_1 and ψ_2, while the label "3" means that electrons in the central well are primarily in state ψ_3. (d) Subband energy ε_ν vs V_B, with the Fermi level pinned at $\varepsilon_F = 189$ meV. Black (empty) circles indicate where the crossing between ε_1 and ε_2 or anticrossing between ε_2 and ε_3 occurs. (e) Rashba α_ν and (f) Dresselhaus β_ν SO coefficients as functions of V_B, with the inset showing a blowup of how SO coefficients vary with V_B near the crossing point. In (d)–(f), the top gate potential is held fixed at zero bias and, in (e) (and inset), the black (solid) circle indicates that all α_ν's of the three subbands identically vanish at $V_B = 0$.

By varying the barrier height of the two inner barriers, which are embedded to form a triple well, dependence

of SO couplings on engineered structures, which are either structurally symmetric or asymmetric, is also discussed (Figs. 4–6). Remarkably, in the latter asymmetric case, through varying V_B we realize a *seemingly* symmetric configuration, in which α_1 and α_2 essentially vanish while α_3 is nonzero, providing a handle for suppressing spin relaxation of electrons of given subbands in a selective manner [Fig. 7(a)].

Moreover, we also determine how the interplay of intra- and interband SO terms affects the energy dispersion. We observe that the two crossings between adjacent subbands for the energy dispersion may remain or turn to avoided crossings, depending on the relative signs of intraband SO terms (Fig. 8). Finally, we also analyze the random Rashba field arising from fluctuation of the concentration of dopant ions [56–58]. Our results should stimulate more experiments probing unusual SO features in multiband and multiwell quantum systems and more proposals designed for spintronic applications and act as a guide for more proposals designed for spintronic devices.

The rest of the paper is structured as follows. In Sec. II, we derive the effective 2D Hamiltonian for electrons in quantum wells with three occupied subbands and present the relevant expressions for the intra- and interband SO interactions. In Sec. III, we first introduce our system and relevant physical parameters adopted, and further present our self-consistent results and discussion. We summarize our main findings in Sec. IV.

II. MODEL AND METHOD

Here we outline the derivation of an effective 2D Hamiltonian for electrons in multisubband quantum wells with both Rashba and Dresselhaus SO interactions. More specifically, we derive an effective 2D Hamiltonian for a three-subband system and determine the relevant SO couplings.

A. From a 3D to an effective 2D Hamiltonian

The 3D Hamiltonian for electrons in the presence of both the Rashba and Dresselhaus SO interactions for quantum wells grown along the $z||[001]$ direction reads [33,59],

$$\mathcal{H}^{3D} = -\frac{\hbar^2}{2m^*}\frac{\partial^2}{\partial z^2} + V(z) + \frac{\hbar^2(k_x^2+k_y^2)}{2m^*} + \mathcal{H}_{\mathcal{R}}^{3D} + \mathcal{H}_{\mathcal{D}}^{3D}, \tag{1}$$

where m^* is the electron effective mass and $k_{x,y}$ the electron momentum along the $x||[100]$ and $y||[010]$ directions. The electron potential $V = V_g + V_w + V_d + V_e$, containing the external gate potential V_g with both top (V_T) and back (V_B) gate contributions [Fig. 1(a)], the structural potential V_w arising from the band offset at the well/barrier interfaces [Fig. 1(b)], the doping potential V_d, and the electron Hartree potential V_e [11,12,18,33]. Note that V is calculated self-consistently within the (Poisson-Schrödinger) Hartree approximation. The terms $\mathcal{H}_{\mathcal{R}}^{3D}$ and $\mathcal{H}_{\mathcal{D}}^{3D}$ describe the Rashba and Dresselhaus SO interactions, respectively. The Rashba term reads $\mathcal{H}_{\mathcal{R}}^{3D} = \eta(z)(k_x\sigma_y - k_y\sigma_x)$, with $\eta(z) = \eta_w\partial_z V_w + \eta_H\partial_z(V_g + V_d + V_e)$ determining the Rashba strength and $\sigma_{x,y,z}$ the spin Pauli matrices. The parameters η_w and η_H involve bulk quantities of materials [18,33,34]. The Dresselhaus contribution has the form $\mathcal{H}_{\mathcal{D}}^{3D} = \gamma[\sigma_x k_x(k_y^2 - k_z^2) + \text{c.c.}]$ with γ the bulk Dresselhaus parameter and $k_z = -i\partial_z$ [22,59].

Now we are ready to define an effective three-subband 2D model from the 3D Hamiltonian [Eq. (1)]. We first determine (self-consistently) the spin-degenerate eigenvalues $\varepsilon_{\mathbf{k}\nu} = \mathcal{E}_\nu + \hbar^2k^2/2m^*$ and the corresponding eigenspinors $|\mathbf{k}\nu\sigma\rangle = |\mathbf{k}\nu\rangle \otimes |\sigma\rangle$, $\langle\mathbf{r}|\mathbf{k}\nu\rangle = \exp(i\mathbf{k}\cdot\mathbf{r})\psi_\nu(z)$, of the well in the absence of SO interaction. Here we have defined $\mathcal{E}_\nu$ (ψ_ν), $\nu = 1, 2, 3$, as the νth quantized energy level (wave function) and $\sigma = \uparrow, \downarrow$ as the electron spin component along the z direction. Then the effective 2D Rashba-Dresselhaus model with three subbands in the coordinate system $[x||(100), y||(010)]$ under the basis set $\{|\mathbf{k}1\uparrow\rangle, |\mathbf{k}1\downarrow\rangle, |\mathbf{k}2\uparrow\rangle, |\mathbf{k}2\downarrow\rangle, |\mathbf{k}3\uparrow\rangle, |\mathbf{k}3\downarrow\rangle\}$ reads $\mathcal{H}^{2D} = \mathcal{H}_0^{2D} + \mathcal{H}_{\mathcal{R}}^{2D} + \mathcal{H}_{\mathcal{D}}^{2D}$, with $\mathcal{H}_0^{2D}$, $\mathcal{H}_{\mathcal{R}}^{2D}$, and $\mathcal{H}_{\mathcal{D}}^{2D}$ the spin-independent part and the Rashba and Dresselhaus SO contributions, respectively,

$$\mathcal{H}_0^{2D} = \begin{pmatrix} \varepsilon_{\mathbf{k}1} & 0 & 0 \\ 0 & \varepsilon_{\mathbf{k}2} & 0 \\ 0 & 0 & \varepsilon_{\mathbf{k}3} \end{pmatrix} \otimes \mathbb{1}, \tag{2}$$

$$\mathcal{H}_{\mathcal{R}}^{2D} = \begin{pmatrix} \alpha_1 & \eta_{12} & \eta_{13} \\ \eta_{12} & \alpha_2 & \eta_{23} \\ \eta_{13} & \eta_{23} & \alpha_3 \end{pmatrix} \otimes (\sigma_y k_x - \sigma_x k_y), \tag{3}$$

$$\mathcal{H}_{\mathcal{D}}^{2D} = \begin{pmatrix} \beta_1 & \Gamma_{12} & \Gamma_{13} \\ \Gamma_{12} & \beta_2 & \Gamma_{23} \\ \Gamma_{13} & \Gamma_{23} & \beta_3 \end{pmatrix} \otimes (\sigma_y k_y - \sigma_x k_x), \tag{4}$$

where $\mathbb{1}$ denotes the 3×3 matrix in both spin and orbital (subband) subspaces and α_ν (β_ν) is the Rashba (Dresselhaus) *intraband* coupling for the νth subband with $\nu = 1, 2, 3$. Here Eqs. (3) and (4) also account for the SO-induced *interband* couplings between subbands μ and ν via the parameters $\eta_{\mu\nu}$ (Rashba) and $\Gamma_{\mu\nu}$ (Dresselhaus) with $\mu \neq \nu$. Note that here there are 12 SO coefficients (α_ν, β_ν, $\eta_{\mu\nu}$, $\Gamma_{\mu\nu}$) in total, while it is straightforward to determine (at least numerically) how these SO terms affect the energy dispersion; see, for instance, Fig. 8 for the three-level Rashba SO dispersion. Also, we have derived an effective 2D Hamiltonian solely for electrons with the explict form (and symmetry) for all Rashba and Dresselhaus terms of both intra- and interband types. This is clearly beyond directly solving the original 8×8 Kane model, from which, although one obtains more precise spin-splitting energy, different kinds of SO contributions may be mixed together.

B. Rashba and Dresselhaus SO coefficients

In Eqs. (3) and (4), the Rashba SO coefficients can be cast as the expectation values $\langle\ldots\rangle$ of the weighted derivatives of the potential contributions,

$$\eta_{\nu\nu'} = \langle\psi_\nu|\eta_w\partial_z V_w + \eta_H\partial_z(V_g + V_d + V_e)|\psi_{\nu'}\rangle, \tag{5}$$

and the Dresselhaus SO strength reads

$$\Gamma_{\nu\nu'} = \gamma\langle\psi_\nu|k_z^2|\psi_{\nu'}\rangle, \tag{6}$$

where we have defined the intraband Rashba $\alpha_\nu \equiv \eta_{\nu\nu}$ and Dresselhaus $\beta_\nu \equiv \Gamma_{\nu\nu}$, as well as the interband Rashba $\eta_{\mu\nu}$ and Dresselhaus $\Gamma_{\mu\nu}$, $\mu \neq \nu$. Note that the intraband Rashba term α_ν can be written in terms of several constituent contributions, i.e., $\alpha_\nu = \alpha_\nu^g + \alpha_\nu^d + \alpha_\nu^e + \alpha_\nu^w$, with $\alpha_\nu^g = \eta_H\langle\psi_\nu|\partial_z V_g|\psi_\nu\rangle$ the gate contribution, $\alpha_\nu^d = \eta_H\langle\psi_\nu|\partial_z V_d|\psi_\nu\rangle$ the doping contribution, $\alpha_\nu^e = \eta_H\langle\psi_\nu|\partial_z V_e|\psi_\nu\rangle$ the electron

Hartree contribution, and $\alpha_\nu^{\rm w} = \eta_{\rm w}\langle\psi_\nu|\partial_z V_{\rm w}|\psi_\nu\rangle$ the structural contribution. Similarly, the interband Rashba term $\eta_{\mu\nu} = \eta_{\mu\nu}^{\rm g} + \eta_{\mu\nu}^{\rm d} + \eta_{\mu\nu}^{\rm e} + \eta_{\mu\nu}^{\rm w}$. For convenience, we also use $\alpha_\nu^{\rm g+d} = \alpha_\nu^{\rm g} + \alpha_\nu^{\rm d}$ and $\eta_{\mu\nu}^{\rm g+d} = \eta_{\mu\nu}^{\rm g} + \eta_{\mu\nu}^{\rm d}$. Even though α_ν and $\eta_{\mu\nu}$ comprise seemingly independent contributions, we note that each of them depends on the total potential V *via* the self-consistent wave function.

III. RESULTS AND DISCUSSION

We first introduce our system and relevant parameters adopted. Then, we show our self-consistent calculations on the Rashba and Dresselhaus SO couplings of both intra- and interband terms for our triple wells with either structurally symmetric or asymmetric configurations. The random Rashba SO effect arising from fluctuations of the concentration of dopant ions is also analyzed.

A. System

We consider the [001]-grown $Ga_{0.47}In_{0.53}As$ wells, which have relatively strong spin-orbit couplings (cf. GaAs) [33,54,55], sandwiched between 48-nm $Al_{0.48}In_{0.52}As$ barriers, with two additional (inner) $Al_xIn_{1-x}As$ layers embedded in the well region to form the triple-well configuration [Fig. 1(a)], favoring flexible control of the electron occupancy of three subbands. The overall width of the well is $w = 48$ nm, comprising three local wells ($Ga_{0.47}In_{0.53}As$) of width $L_{\rm w} = 8$ nm separated by two inner barriers ($Al_xIn_{1-x}As$) of width $L_{\rm b} = 12$ nm. Two doping layers of width 1 nm sit 17 nm away from either side of the well, with the doping density $\rho_a = \rho_b = 4\times10^{18}$ cm^{-3}, i.e., symmetric doping condition. The temperature is $T = 0.3$ K and the Fermi level in our simulation is pinned at $\varepsilon_{\rm F} = 189$ meV. Two independent gate potentials $V_{\rm T}$ (top gate) and $V_{\rm B}$ (back gate) are adopted for adjusting the electron occupancy and the symmetry of the system. Without lack of generality, we hold the top gate fixed at zero bias, i.e., $V_{\rm T} = 0$ (reference point), and adjust $V_{\rm B}$ to explore the gate control of SO terms.

In Fig. 1(b), we show the structural potential profile $V_{\rm w}$ (Sec. II) for our triple well illustrated in Fig. 1(a). We focus on both structurally symmetric and asymmetric configurations. In the former case, three cases of inner offsets are considered, with $\delta_2 = \delta_2' = 0.17$, 0.34, and 0.52 eV, where the matching of the left and right inner barrier heights, i.e., $\delta_2 = \delta_2'$, ensures that the system is structurally symmetric. Regarding the latter case, we consider $\delta_2 = 0.34$ eV and $\delta_2' = 0.17$ eV. For realistic considerations, we follow Ref. [60] and determine a mapping between the inner offset and concentration x of the $Al_xIn_{1-x}As$ layer for the values of δ_2 (δ_2') considered in Figs. 1–6, with $\delta_2 = 0.17$, 0.34, and 0.52 eV corresponding to x equal to 0.07, 0.20, and 0.40, respectively. And, the outer offset at the $Ga_{0.47}In_{0.53}As/Al_{0.48}In_{0.52}As$ interfaces is $\delta_1 = 0.52$ eV [18,60].

Below we analyze our calculated SO couplings for the corresponding quantum systems introduced above. We first focus on symmetric wells in which the left and right inner barrier heights are matched.

B. Symmetric well: Intraband SO couplings

Before looking into gate controlled SO couplings, we first examine our self-consistent outcome. In Fig. 1(c), we show the zero-bias self-consistent potential V and wave function profiles ψ_ν ($\nu = 1, 2, 3$) for our symmetric triple well with the inner offsets of $\delta_2 = \delta_2' = 0.17$ eV. We observe that both the first- and second-subband electrons are apt to *reside* in the two outer wells, with no priority of the left or right one (cf. ψ_1 and ψ_2), as indicated by the label "1+2," since the overall system is in the symmetric configuration. The large overlap of spatial distributions between ψ_1 and ψ_2 implies that the subband energy levels ε_1 and ε_2 are basically degenerate. Physically, this follows from the fact that the left and right local wells are largely separated by the two inner barriers and the central well [Fig. 1(b)], which suppress the wave function penetration and further quench the coupling of the two outer wells. Regarding the third subband, its energy level ε_3 is about 10 meV above ε_2 of the second subband, and electrons are preferably localized in the central well (see label "3" and ψ_3), in which the potential energy is higher than that in the left and right wells primarily due to the presence of the electron Hartree potential.

Now we switch on the back gate potential $V_{\rm B}$, which breaks the structural inversion symmetry of the well, to explore how the self-consistent outcome evolves for the system away from the symmetric configuration. Figure 1(d) shows the subband energy levels ε_ν as a function of $V_{\rm B}$, with the Fermi level pinned at $\varepsilon_{\rm F} = 189$ meV [12]. Clearly, the potential energy of the overall system including all the subband energy levels shall be lifted up as $V_{\rm B}$ increases. Since $V_{\rm B}$ is applied on the right of the structure [Figs. 1(a) and 1(b)], electrons confined in the right well react more sensitively in energy increment than those localized in the central and left (local) wells.

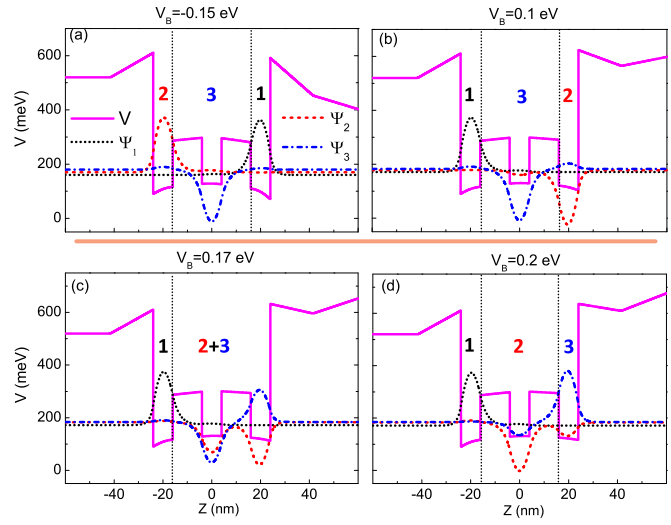

FIG. 2. Self-consistent potential V and wave function profiles ψ_ν for a symmetric triple well with $\delta_2 = \delta_2' = 0.17$ eV, at $V_{\rm B} = -0.15$ (a), 0.1 (b), 0.17 (c), and 0.2 eV (d). The top gate $V_{\rm T}$ is held fixed at zero bias. The labels "ν" ($\nu = 1, 2, 3$) inside the well region mean where electrons occupying the νth subband are localized and "3+2" in (c) indicates that electrons confined in the central and right local wells are in states of both ψ_2 and ψ_3.

This leads to a crossing of the energy levels ε_1 and ε_2 near the symmetric configuration (across $V_B = 0$), indicating the essential degeneracy between the first and second subbands aforementioned. Further, when the gate potential increases to $V_B \approx 0.17$ eV, there is an emergent anticrossing between energy levels ε_2 and ε_3 respectively for the second and third subbands. The avoided crossing arises from the appreciable coupling of the involved subbands, in contrast to the scenario of the energy-level crossing at zero bias, as we will analyze in detail later on. Despite the distinction of the crossing and anticrossing of energy levels, either of the cases reflects the occurrence of band swapping. Namely, we achieve the intriguing double band swapping simply by just adjusting V_B. These self-consistent features of triple wells are helpful in understanding our calculated SO couplings.

Figures 1(e) and 1(f) show the gate dependence of intraband Rashba (α_ν) and Dresselhaus (β_ν) SO couplings, respectively, as functions of V_B, for our symmetric triple well with $\delta_2 = \delta_2' = 0.17$ eV. We observe an emerging double interchange of the Rashba (Dresselhaus) SO coefficients as V_B varies, i.e., the SO interchange of the first-subband α_1 (β_1) and second-subband α_2 (β_2) near the crossing point ($V_B = 0$) and further of the second-subband α_2 (β_2) and third-subband α_3 (β_3) near the anticrossing point ($V_B \approx 0.17$ eV), which is greatly fascinating for selective SO control among distinct subbands in spintronic devices. The intriguing double-interchanging feature of nonlinear SO control follows exactly from our self-consistent outcome of the double band swapping aforementioned.

Strictly speaking, we should emphasize that the Dresselhaus SO terms β_1 and β_2 have already undertaken a double interchange even near the crossing point ($V_B = 0$), in contrast to the Rashba SO contributions; cf. the insets in Figs. 1(e) and 1(f). However, this is a minor effect with a variation of only about 1%, allowing us to identify the *actual* double interchange as an *effective* single SO interchange for the Dresselhaus SO strength near $V_B = 0$. In addition, it is found that α_3 maintains the usual linear behavior near the crossing point, while α_1 obeys the linear gate dependence around the anticrossing point, similarly for the gate control of β_3 and β_1 near the crossing and anticrossing points, respectively. Note that, right at the crossing point, the system is structurally symmetric, and hence α_ν for all the three subbands identically vanishes, as indicated by the black (solid) circle. Further, it is striking that here we also realize a wide-range gate control of Dresselhaus SO terms, which usually depend on quantum confinement while being immune to electrical manipulation [12]. Thus a triple-well configuration offers a promising candidate for a simultaneous control of both Rashba and Dresselhaus SO terms through electrical means.

Having the basic SO features analyzed above, we are now ready to discuss more deeply the Rashba SO terms, which also involve a sign reversal. From Fig. 1(e), it is found that α_1 and α_2 maintain opposite signs. Further, α_1 and α_2 remain essentially constant when $V_B > 0$ and $V_B < 0$, respectively, providing a handle for independent control of SO terms of distinct subbands, i.e., adjusting α_1 while essentially holding α_2 fixed at a constant, or vice versa. Also, for the third subband, the SO strength is much smaller than that of the first and second subbands, and exhibits weak gate dependence, within a broad range of V_B considered. To clarify these features, we have to reexamine our self-consistent outcome in more detail, involving electrically controlled redistribution of electrons occupying the three subbands among the three local (left, central, and right) wells [Fig. 1(b)], as we discuss next.

In Figs. 2(a)–(d), we show our self-consistent potential and wave function profiles for our symmetric triple well at $V_B = -0.15$, 0.1, 0.17, and 0.2 eV, respectively. This allows us to analyze how the spatial distribution for electrons of the three subbands that evolve among the left, central, and right wells as V_B varies. At zero bias, the overall system with $\delta_2 = \delta_2'$ is structurally symmetric, and hence there is no priority for electrons to be localized in the left or right well. This leads to basically the same distribution of ψ_1 or ψ_2 in the left and right wells [Fig. 1(c)], implying the essential degeneracy of the first and second subbands [Fig. 1(d)]. On the other hand, for ψ_3 of the third subband, it is mainly confined in the central well [Fig. 1(c)].

When V_B deviates from zero bias, the intrinsic structural inversion symmetry is broken and further the degeneracy associated with the right and left wells is lifted, with the right well lower (higher) than the left one for V_g less (greater) than zero; cf. Figs. 2(a) and 2(b) for $V_B = -0.15$ and 0.1 eV, respectively. Accordingly, when $V_B = -0.15$ eV, electrons occupying the first subband are opt to be localized in the right well, while for the second subband electrons preferably reside in the left one [Fig. 2(a)]. Clearly, the scenario is the opposite when $V_B = 0.1$ eV [Fig. 2(b)]; cf. ψ_1 and ψ_2 at $V_B = -0.15$ and 0.1 eV. This indicates that the band swapping of the first and second subbands near the symmetric configuration is accompanied with a distribution exchange of ψ_1 and ψ_2 between the left and right wells. Thus a sign flip of α_1 and α_2 follows since the local force fields (i.e., derivative of potential with respect to z) in the left and right wells have opposite signs. Moreover, the left well, which is far away from where the back gate V_B is applied as compared to the left and central wells, is not sensitive to energy lifting as V_g increases, giving rise to α_1 and α_2 remaining essentially constant when $V_B > 0$ and $V_B < 0$, respectively. Further, because of the local symmetry in the central well, α_3 is relatively small and exhibits weak gate dependence over a broad range of V_B considered.

When V_B further increases from 0.1 eV, the energy separation between the second and third subbands, with the corresponding wave functions mostly confined in the right and central wells, respectively, gradually quenches, as a result of the right well reacting more sensitively in energy increments than the central one with increasing V_B. This leads to spatial redistributions of the second- and third-subband electrons between the central and right wells. Specifically, as V_B increases, the second-subband electrons confined in the right well tend to *move* to the central one, while for electrons occupying the third subband the scenario is the opposite. At $V_B = 0.17$ eV, ψ_2 and ψ_3 are largely overlapped in the central and right wells [Fig. 2(c)]. When V_B increases to 0.2 eV, they are basically separately localized in the central and right wells with a minor overlap [Fig. 2(d)]. The band anticrossing between ε_2 and ε_3 arises from the considerable coupling between the adjacent central and right wells. This is in contrast to the band crossing between ε_1 and ε_2 at $V_B = 0$, as the coupling between the

two outer (left and right) wells, which are largely separated, is much weaker. Therefore, detailed interchanging features of nonlinear SO control near the crossing and anticrossing points are also contrasting. In the latter case of considerable coupling between adjacent local wells, the yielding SO interchange spreads a broad gate range; cf. SO features near the crossing and anticrossing points of Figs. 1(e) and 1(f).

Very recently, based on the idea of the charge transfer among the three local wells, a gate-voltage-induced switching of spin relaxation and an efficient on:off ratio of the current in spin-field-effect transistor was proposed [53]. In this proposal, the key is that the Rashba coefficient for electrons localized in the central well due to the local symmetry is much weaker than that in the right or left local wells, consistent with our predictions; cf. α_3 and α_1 (or α_2). Also, strong anisotropy of the spin relaxation time and long spin transport length (exceeding a half millimeter) were revealed in GaAs triple wells [47–49]. These all indicate that a triple-well configuration favoring electron occupancy of three subbands offers more possibilities for the SO control and spintronic applications.

C. Symmetric well: Interband SO couplings

Now we move to the gate controlled interband SO terms, as shown in Figs. 3(a) and 3(b) for the Rashba ($\eta_{\mu\nu}$) and Dresselhaus ($\Gamma_{\mu\nu}$) SO couplings, respectively. We first have a look at the band-swapping mediated interband Rashba SO terms near the crossing point (zero bias). We observe that η_{12} and η_{23} exhibit maximal magnitudes at $V_B = 0$, i.e., a *resonant* behavior with V_B near the symmetric configuration, as also highlighted in the inset, in contrast to η_{13} and intraband terms α_ν which identically vanish at zero bias. This is attributed to distinct parities of relevant wave functions and their corresponding spatial overlap. More specifically, since the wave functions of both the first (ψ_1) and third (ψ_3) subbands have the even parity, the gate dependence of η_{13} is expected to be similar to that of intraband α_ν terms. Considering that the Rashba SO terms involve the force fields [Eq. (5)], a vanishing η_{13} follows at the crossing point for the well in the symmetric configuration. As for η_{12} (η_{23}), since the wave functions of ψ_2 and ψ_1 (ψ_3) are largely overlapped at $V_B = 0$, a resonance for its gate dependence across the symmetric configuration directly occurs. Near the anticrossing point, which is away from the symmetric configuration and involves the band swapping of the second (ψ_2) and third (ψ_3) subbands, the interband Rashba SO features are dominated by the overlap of associated wave functions or the coupling of relevant local wells, instead of the parity of wave function. As a result, η_{12} and η_{13} interchange the values, while η_{23} displays the resonant feature with V_B.

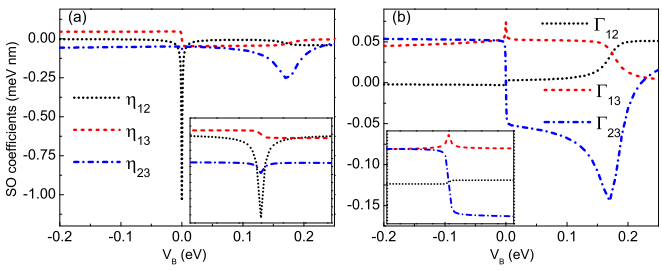

FIG. 3. Interband Rashba $\eta_{\mu\nu}$ (a) and Dresselhaus $\Gamma_{\mu\nu}$ (b) SO coefficients for the symmetric triple well of $\delta_2 = \delta_2' = 0.17$ eV, with $\mu, \nu = 1, 2, 3$ and $\mu \neq \nu$, as functions of V_B. In (a), the inset shows a blowup of how $\eta_{\mu\nu}$ varies with V_B near the crossing point, where the magnitude of η_{23} is enhanced by a factor of seven for highlighting its *resonant* behavior. The top gate potential is pinned at $V_T = 0$.

Regarding the interband Dresselhaus SO couplings, which have nothing to do with the derivative of confining potentials [Eq. (6)], we find that the interband term Γ_{13} between the first and third subbands exhibits the maximal magnitude near the symmetric configuration, while Γ_{12} (Γ_{23}) between the second and first (third) subbands identically vanishes because of distinct parities of the involved subbands. This is in stark contrast to the interband Rashba SO terms; cf. $\eta_{\mu\nu}$ and $\Gamma_{\mu\nu}$. On the other hand, near the anticrossing point, the interchanging feature of Dresselahus SO terms is also dominated by the overlap of associated wave functions or the coupling of relevant local wells, similar to that of Rashba SO terms.

We should emphasize that the interband terms may have various SO effects, including the avoided crossings of band dispersion [37], intrinsic spin Hall effect [38,61], spin filtering [62], and unusual *zitterbewegung* [63,64]. Also, an efficient spin-filter device was proposed based on the triple-well structure [52]. Further, a rapid change of SO coefficients (both intra- and interband terms) near the crossing or anticrossing points is in favor of realizing efficient switching of an on-to-off state, which is greatly promising for spin-transistor devices.

D. Symmetric well: Inner-barrier-height engineering

In the following, we focus on how the inner-barrier height affects the aforementioned SO features for our symmetric triple well with $\delta_2 = \delta_2'$. In Fig. 4, we show the gate dependence of intraband Rashba α_ν [(a)–(c)] and Dresselhaus β_ν [(d)–(f)] for symmetric wells at several values of inner barrier heights of $\delta_2 = 0.17$, 0.34, and 0.52 eV. The intraband Rashba SO coupling α_ν, which mainly depends on the structural inversion asymmetry of the system, in general has weak dependence on δ_2. However, a striking feature is that the gate range covering the interchanging feature of α_2 and α_3 near the anticrossing point becomes greatly quenched as δ_2 increases; cf. α_2 (α_3) at $\delta_2 = 0.17$, 0.34, and 0.52 eV. This indicates that the avoided crossing between the energy levels of the second and third subbands [Fig. 1(d)] gradually turns to crossing with increasing inner offsets, which suppress the penetration of wave function and further quench the coupling between the right and central wells, as indicated in the inset of Fig. 4(a) for ψ_1, ψ_2, and ψ_3. These wave functions are mostly confined in the left, right, and central wells, respectively, and are essentially spatially separated.

Since a larger inner-barrier height greatly suppresses the wave-function penetration, the Dresselhaus SO terms, which mainly depend on quantum confinement, have much stronger dependence on δ_2 than the Rashba ones; cf. α_ν and β_ν. This offers a means for selective SO control between Rashba and Dresselhaus terms by engineering the inner-barrier heights. On the one hand, β_ν grows with increasing δ_2; cf. dotted, dashed, and dash-dotted curves; on the other hand, the gate dependence of β_ν becomes suppressed for a larger δ_2.

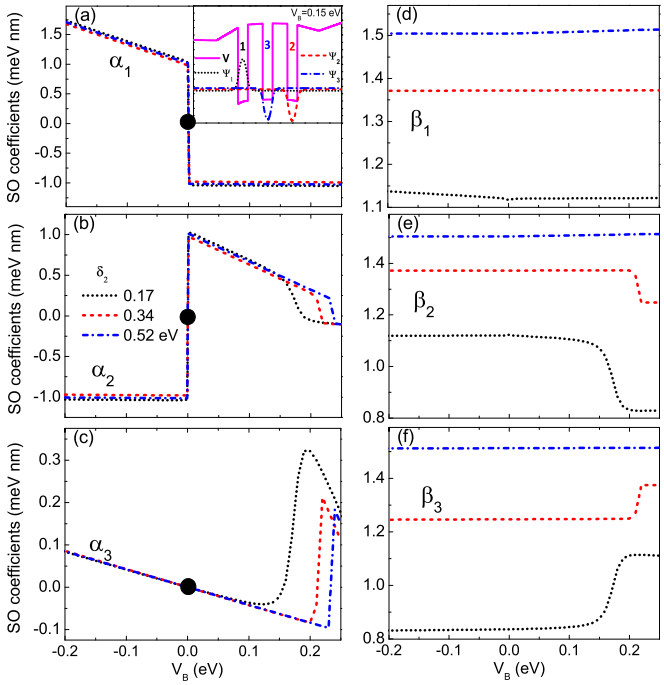

FIG. 4. Rashba α_ν [(a)–(c)] and Dresselhaus β_ν [(e)–(f)] for symmetric triple wells at several values of left inner-barrier height $\delta_2 = 0.17$, 0.34, and 0.52 eV, as functions of V_B. The right inner-barrier height obeys $\delta_2' = \delta_2$ so that the overall system is symmetric at zero bias [see Fig. 1(b)]. The top gate potential is pinned at $V_T = 0$. In (a), the inset shows the self-consistent potential V and wave function profiles ψ_ν at $V_B = 0.15$ eV, with the labels "ν" ($\nu = 1, 2, 3$) inside the well region meaning where electrons occupying the νth subband are localized. The black (solid) circle in (a)–(c) indicates that α_ν vanishes at $V_B = 0$.

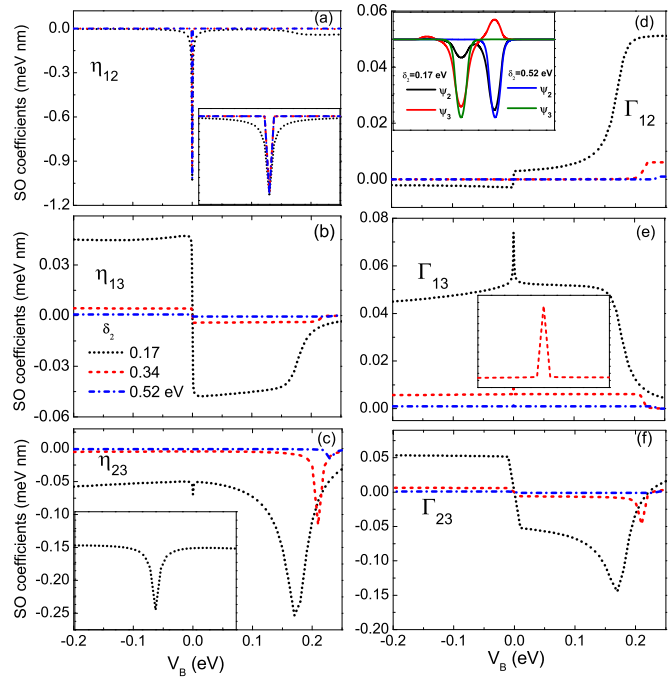

FIG. 5. Back gate V_B dependence of interband Rashba $\eta_{\mu\nu}$ [(a)–(c)] and Dresselhaus $\Gamma_{\mu\nu}$ [(e)–(f)] SO couplings for symmetric triple wells at several values of inner-barrier height with $\delta_2 = \delta_2' = 0.17$, 0.34, and 0.52 eV, where the equal height for left (δ_2) and right (δ_2') inner barriers ensures that the overall system is symmetric at zero bias [see Fig. 1(b)]. In (d), the inset illustrates spatial distributions of ψ_1 and ψ_2 for the triple well with $\delta_2 = 0.1$ and 0.52 eV at $V_B = 0.1$ eV. The top gate is held fixed at $V_T = 0$ in the whole gate range of V_B considered.

Figure 5 shows the corresponding interband Rashba $\eta_{\mu\nu}$ [(a)–(c)] and Dresselhaus $\Gamma_{\mu\nu}$ [(d)–(f)] SO couplings as functions of V_B for $\delta_2 = 0.17, 0.34$, and 0.52 eV, respectively. Since the interband terms $\eta_{\mu\nu}$ and $\Gamma_{\mu\nu}$ strongly depend on the overlap of the μth (ψ_μ) and νth (ψ_ν) subband wave functions, both of them in general decrease with increasing δ_2. To better appreciate that the inner barriers quench the overlap of wave functions of distinct subbands, we show in the inset of Fig. 5(d) ψ_1 and ψ_2 for our triple well with $\delta_2 = 0.17$ and 0.52 eV at $V_B = 0.15$ eV. Clearly, there is almost no overlap between ψ_1 and ψ_2 when $\delta_2 = 0.52$ eV. As a consequence, either η_{12} or Γ_{12} remains essentially vanishing when V_B is nonzero. Note that, for all values of δ_2's, right in the symmetric configuration at $V_B = 0$, η_{12} exhibits a resonance; following from that the states of the first (ψ_1) and second (ψ_2) subbands are essentially degenerate. As opposed to η_{12}, Γ_{12} is vanishing at $V_B = 0$ because of distinct parities of ψ_1 and ψ_2.

E. Asymmetric well: Unmatched left and right inner barrier heights

In this section, we turn to an intrinsically asymmetric triple well, in which the left inner-barrier height δ_2 is not matched with the right one δ_2' [Fig. 1(b)]. In Fig. 6(a), we show the zero-bias self-consistent potential V and wave function profiles ψ_ν for an asymmetric well with $\delta_2 = 0.34$ eV and $\delta_2' = 0.17$ eV. Even at zero bias, we find that the wave functions of the three subbands, ψ_1, ψ_2, and ψ_3, are mostly localized in the right, left, and central local wells, respectively, due to the intrinsic asymmetry between the left and right local wells. This is in stark contrast to the scenario for the symmetric well at $V_B = 0$, where either ψ_1 or ψ_2 has similar spatial distributions in the left and right wells; cf. Figs. 1(c) and 6(a). Interestingly, by tuning the back gate potential, we achieve a *seemingly* symmetric configuration at $V_B \approx 0.03$ eV, as shown in Fig. 6(b), in which ψ_1 and ψ_2 are largely overlapped in the left and right local wells.

Figure 6(c) shows how the subband energy levels ε_ν evolve as V_B varies. Similar to the case of the symmetric well, we also achieve the double band swapping by varying V_B, i.e., the crossing between ε_1 and ε_2 and the anticrossing between ε_2 and ε_3. Note that, since the well is now intrinsically asymmetric, the crossing point does not take place at zero bias, in contrast to the symmetric well; cf. Figs. 2(b) and 6(b). Instead, the crossing point occurs at $V_B \approx 0.03$ eV, corresponding to our triple well in the *seemingly* symmetric configuration emphasized above.

In Figs. 7(a) and 7(b), we show the intraband Rashba α_ν and Dresselhaus β_ν SO couplings as functions of V_B. Due to the occurrence of the double band swapping, α_ν and β_ν also exhibit features of double SO interchange when V_B is adjusted. However, because of the shift of the crossing point from zero bias, remarkably we observe that α_1 and α_2 essen-

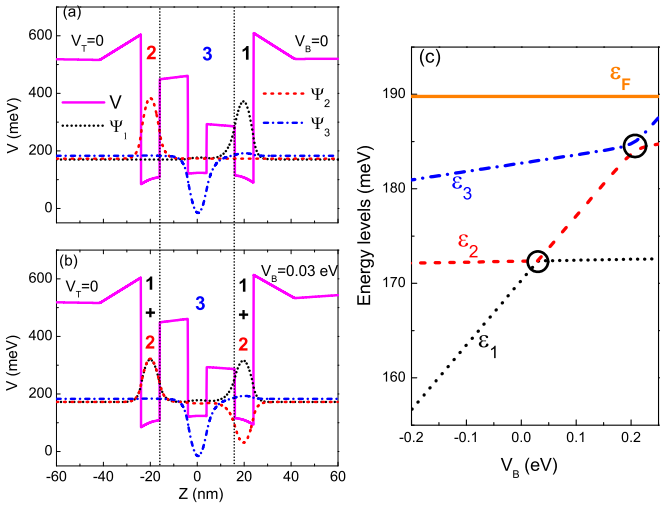

FIG. 6. Self-consistent potential V and wave function profiles of ψ_ν for an asymmetric triple well with $\delta_2 = 0.34$ eV and $\delta_2' = 0.17$ eV, which embraces intrinsic symmetric breaking due to unmatched δ_2 and δ_2' [see Fig. 1(b)], at $V_B = 0$ (a) and 0.03 eV (b). The labels "ν" ($\nu = 1, 2, 3$) inside the well region mean where electrons occupying the νth subband are localized, and the label "1+2" indicates that electrons in the left and right local wells are predominantly in states of both ψ_1 and ψ_2. (c) Back gate V_B dependence of the energy levels ε_ν. The Fermi level is pinned at $\varepsilon_F = 189$ meV, and the black (empty) circles indicate where the crossing between ε_1 and ε_2 or the anticrossing between ε_2 and ε_3 takes place. The top gate potential V_T is held fixed at zero bias.

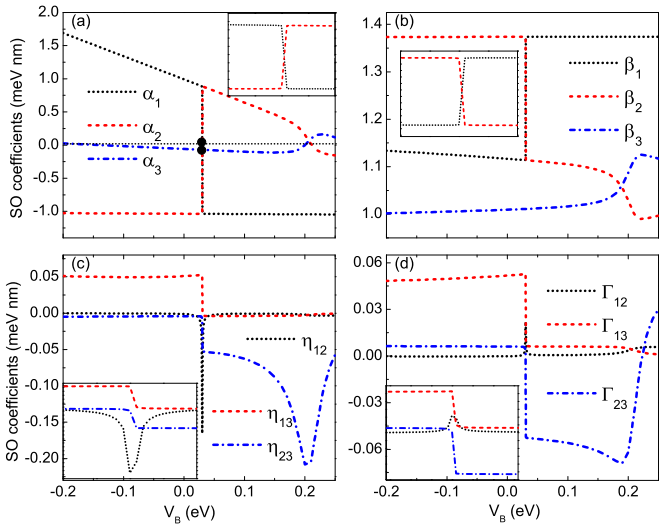

FIG. 7. Intraband Rashba α_ν (a) and Dresselhaus β_ν (b) and interband Rashba $\eta_{\mu\nu}$ (c) and Dresselhaus $\Gamma_{\mu\nu}$ (d) SO coefficients for the asymmetric triple well with $\delta_2 = 0.34$ eV and $\delta_2' = 0.17$ eV as functions of V_B. In (a)–(d), the inset shows a blowup of the corresponding SO coefficients near the crossing point $V_B \approx 0.03$ eV, in contrast to the symmetric well with the crossing point taking place at zero bias; cf. Figs. 1(d) and 6(c). The black (solid) circles in (a) and the inset indicate that α_1 and α_2 essentially vanish while α_3 is nonzero, for which the system is under a *seemingly* symmetric configuration illustrated in Fig. 6(b).

tially vanish while α_3 is nonzero [see black circles in Fig. 7(a) and its inset], in contrast to the symmetric triple well, where all α_ν's of the three subbands are zero at the crossing point. Here the essential vanishing of Rashba coefficients of the first and second subbands arises from the compensated symmetry breaking between the external gate potential and the intrinsic unmatched left and right inner barrier heights.

Concerning the interband Rashba $\eta_{\mu\nu}$ and Dresselhaus $\Gamma_{\mu\nu}$ SO couplings, the corresponding gate dependences are shown in Figs. 7(c) and 7(d), respectively. Near band-swapping points, $\eta_{\mu\nu}$ and $\Gamma_{\mu\nu}$ exhibit either a *resonant* behavior or a steplike jump with V_B, similar to symmetric wells.

F. Energy dispersion of three-subband spin branches

Figure 8 shows the energy dispersion of distinct spin branches for the three occupied subbands with both intra- and interband Rashba SO terms. We mainly focus on the two crossings at $k_x > 0$ between adjacent subbands when the interband SO terms ($\eta_{\mu\nu}$) are absent, i.e., between the first subband (upper branch) and second subband (lower branch) and between the second subband (upper branch) and the third subband (lower branch), respectively; see black circles in Fig. 8(a). We reveal that the interband terms may maintain the two crossings or give rise to avoided crossings, depending on the relative signs of the intraband SO constants. More specifically, when all the α's of intraband terms have the same sign, both of the two crossings remain even for finite $\eta_{\mu\nu}$, with the crossing points shifted; cf. Figs. 8(a) and 8(b). Interestingly, when the sign of α_2 is reversed, the two crossings simultaneously turn to avoided crossings; cf. Figs. 8(b) and 8(c). The underlying physics is attributed to the fact that the Rashba interband terms only couple different branches with the same spin. Similar features occur for the energy dispersion of multiband Dresselhaus SO terms (not shown). We should emphasize that the energy dispersion becomes more complex in the presence of both Rashba and Dresselhaus SO terms for the three-level system. More work is needed to dig into these features as well as the corresponding hybridized spin textures among distinct spin branches.

G. Random Rashba SO contribution

In general, the intraband Rashba SO coupling in systems with no structural inversion symmetry vanishes. However, the Rashba coupling vanishes only on average and electrons are still subject to a spatially fluctuating Rashba field [56,58], i.e., a random Rashba term, which arises from fluctuations of the concentration of dopant ions [56–58,66,67]. The random Rashba effect is usually small in GaAs-based wells [12,33], while it may become important in InSb narrow-gap semiconductors [33], in which a large SO constant may potentially enhance the random Rashba contribution.

We follow Ref. [56] and evaluate the averaged random Rashba SO strength $\sqrt{\langle \alpha_R^2 \rangle} = e^2 \xi \sqrt{\pi n_d}/4\pi\epsilon R_d$, with the subscript R indicating the random contribution. Here e is the electron charge, ϵ denotes the dielectric constant, R_d refers to the distance from the doping region to the well center, and $\xi = \eta_H - \eta_w$ [12,33]. As electrons of the three subbands see the same doping conditions, fluctuations of the Rashba cou-

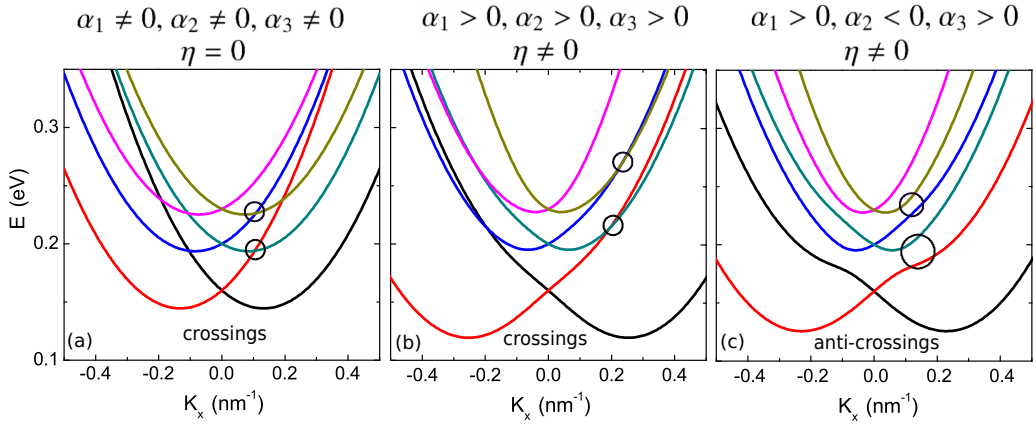

FIG. 8. Energy dispersions along $k_x \parallel [100]$ of an AlInAs/GaInAs triple well with $\delta_2 = 0.17$ eV, for $\alpha_{1,2,3} \neq 0$, $\eta_{\mu\nu} = 0$ (a), $\alpha_{1,2,3} > 0$, $\eta \neq 0$ (b), and $\alpha_{1,3} > 0$, $\alpha_2 < 0$ (c). In (a), double crossings at $k_x > 0$ [65] occur when different subbands are decoupled (i.e., $\eta_{\mu\nu=0}$); see black circles. The two crossings may remain when all α's have the same sign or both of them turn to avoided crossings when the sign of α_2 is reversed. The SO constants are chosen at $V_B = 0.1$ eV [see Fig. 1(e)] and scaled up by two orders for visibility.

plings are assumed the same in both subbands, i.e., $\sqrt{\langle\alpha_{1,R}^2\rangle} = \sqrt{\langle\alpha_{2,R}^2\rangle} = \sqrt{\langle\alpha_{3,R}^2\rangle}$. For our triple wells, the areal doping density reads $n_d \sim \rho_d l_d = 8 \times 10^{11}$ cm^{-2}, where $\rho_d = 3 \times 8^{18}$ cm^{-3} is the three-dimensional doping concentration and $l_d = 1$ nm stands for the length of doping layers. This yields a variation of the Rashba SO couplings $\sqrt{\langle\alpha_{v,R}^2\rangle} \sim 0.14$ meV nm. Although the random contribution is much weaker than the usual contributions α_1 and α_2 that we calculated for the first two subbands, it is comparable to α_3 for the third subband; see Fig. 1(e). Note that, although the random Rashba effect will not change the general SO features driven by the band crossing and anticrossing, it may play an important role in SO related applications, e.g., the state of persistent spin helix [24,29–31], in which the Rashba and Dresselhaus SO strengths have compensated strengths. Depending on specific applications, one can enhance (quench) the random Rashba effect by increasing (decreasing) the doping concentration and/or by setting the doping region near to (distant from) the well region [Fig. 1(a)].

IV. CONCLUDING REMARKS

Considering current research interest in multisubband quantum systems, we have explored the Rashba and Dresselhaus SO couplings in AlInAs/GaInAs triple wells subjected to top (V_T) and back (V_B) gate potentials, allowing for flexible triple-occupancy control for electrons. By performing a self-consistent Poisson-Schrödinger calculation, we determine all the relevant Rashba (Dresselhaus) SO terms of both intraband α_v (β_v) and interband $\eta_{\mu\nu}$ ($\Gamma_{\mu\nu}$) kinds in both structurally symmetric and asymmetric wells.

For a structurally symmetric triple well, we achieve either the band crossing or anticrossing accompanied by a double band swapping, simply *via* adjusting V_B. As a direct consequence, a double SO interchange occurs as V_B varies, which is greatly fascinating for selective SO control among distinct subbands in spintronic devices. Further, even near the two band-swapping points, across which electrons occupying the three subbands are redistributed among the three different (left, central, and right) local wells (triple well), detailed interchanging features of nonlinear SO control are also contrasting, following from distinct coupling strengths between involved subbands. Regarding the interband Rashba and Dresselhaus SO contributions, $\eta_{\mu\nu}$ and $\Gamma_{\mu\nu}$ exhibit either a *resonant* behavior or a *steplike* jump across band-swapping points, depending on the parity and spatial distribution of electron wave functions. By varying the barrier height of the two inner barriers embedded to form triple-well configuration, which is either structurally symmetric or asymmetric, we find that the Dresselhaus SO terms exhibit much stronger dependence on the engineered structures than the Rashba ones. Interestingly, in the structurally asymmetric well, we realize an intriguing *seemingly* symmetric configuration by varying V_B, in which the intraband Rashba terms α_v for the first and second subbands vanish, while for the third subband it is nonzero, offering a handle for suppressing SO-induced spin relaxation mechanisms in subband controlled systems. Our results should stimulate experiments probing unusual SO features in multiband and multiwell quantum systems and act as a guide for more proposals designed for spintronic applications. Two final remarks: (i) throughout the work we hold the top gate fixed at zero bias and only adjust the back; a dual-gate manipulation may offer more flexible multiband SO control [68,69]; (ii) the Rashba and Dresselhaus interband SO terms may yield new features of spin textures due to the crossings and anticrossings of six spin branches. More work is needed to investigate these possibilities.

ACKNOWLEDGMENTS

This work was supported by the National Natural Science Foundation of China (Grant No. 11874236), the Major Basic Program of Natural Science Foundation of Shandong Province (Grant No. ZR202105280001), and the QFNU research fund. W.L. was also partially supported by the Higher Educational Youth Innovation Science and Technology Program of Shandong Province (Grant No. 2019KJJ010) and the research program of JNXY. One of the authors (J.Y.F.) thanks G. J. Ferreira for helpful discussions about the long spin transport length in triple wells with three occupied subbands.

[1] S. A. Wolf, D. D. Awschalom, R. A. Buhrman, J. M. Daughton, S. von Molnár, M. L. Roukes, A. Y. Chtchelkanova, and D. M. Treger, Spintronics: A spin-based electronics vision for the future, Science **294**, 1488 (2001).

[2] D. Awschalom, D. Loss, and N. Samarth, *Semiconductor Spintronics and Quantum Computation* (Springer, New York, 2002).

[3] I. Žutić, J. Fabian, and S. D. Sarma, Spintronics: Fundamentals and applications, Rev. Mod. Phys. **76**, 323 (2004).

[4] D. Xiao, G. B. Liu, W. X. Feng, X. D. Xu, and W. Yao, Coupled Spin and Valley Physics in Monolayers of MoS_2 and Other Group-VI Dichalcogenides, Phys. Rev. Lett. **108**, 196802 (2012).

[5] J. Y. Fu, A. Bezerra, and F. Y. Qu, Valley dynamics of intravalley and intervalley multiexcitonic states in monolayer WS_2, Phys. Rev. B **97**, 115425 (2018).

[6] J. Y. Fu, J. M. R. Cruz, and F. Y. Qu, Valley dynamics of different trion species in monolayer WSe_2, Appl. Phys. Lett. **115**, 082101 (2019).

[7] B. A. Bernevig, T. L. Hughes, and S. C. Zhang, Quantum spin Hall effect and topological phase transition in HgTe quantum wells, Science **314**, 1757 (2006).

[8] R. M. Lutchyn, J. D. Sau, and S. Das Sarma, Majorana Fermions and a Topological Phase Transition in Semiconductor-Superconductor Heterostructures, Phys. Rev. Lett. **105**, 077001 (2010).

[9] Y. Oreg, G. Refael, and F. von Oppen, Helical Liquids and Majorana Bound States in Quantum Wires, Phys. Rev. Lett. **105**, 177002 (2010).

[10] H. M. Weng, C. Fang, Z. Fang, B. A. Bernevig, and X. Dai, Weyl Semimetal Phase in Noncentrosymmetric Transition-Metal Monophosphides, Phys. Rev. X **5**, 011029 (2015).

[11] J. Y. Fu, P. H. Penteado, M. O. Hachiya, D. Loss, and J. C. Egues, Persistent Skyrmion Lattice of Noninteracting Electrons with Spin-Orbit Coupling, Phys. Rev. Lett. **117**, 226401 (2016).

[12] F. Dettwiler, J. Y. Fu, S. Mack, P. J. Weigele, J. C. Egues, D. D. Awschalom, and D. M. Zumbühl, Stretchable Persistent Spin Helices in GaAs Quantum Wells, Phys. Rev. X **7**, 031010 (2017).

[13] P. J. Weigele, D. C. Marinescu, F. Dettwiler, J. Fu, S. Mack, J. C. Egues, D. D. Awschalom, and D. M. Zumbuhl, Symmetry breaking of the persistent spin helix in quantum transport, Phys. Rev. B **101**, 035414 (2020).

[14] Q. X. Wang, H. Yang, and J. Y. Fu, Selective asymmetric gate control of the Rashba spin-orbit coupling in GaInAs/AlInAs stepped wells, Phys. Rev. B **101**, 245403 (2020).

[15] F. Nichele, M. Kjaergaard, H. J. Suominen, R. Skolasinski, M. Wimmer, B. M. Nguyen, A. A. Kiselev, W. Yi, M. Sokolich, M. J. Manfra, F. Qu, A. J. A. Beukman, L. P. Kouwenhoven, and C. M. Marcus, Giant Spin-Orbit Splitting in Inverted InAs/GaSb Double Quantum Wells, Phys. Rev. Lett. **118**, 016801 (2017).

[16] J. Nitta, T. Akazaki, H. Takayanagi, and T. Enoki, Gate Control of Spin-Orbit Interaction in an Inverted $In_{0.53}Ga_{0.47}As/In_{0.52}Al_{0.48}As$, Phys. Rev. Lett. **78**, 1335 (1997).

[17] D. Grundler, Large Rashba Splitting in InAs Quantum Wells due to Electron Wave Function Penetration into the Barrier Layers, Phys. Rev. Lett. **84**, 6074 (2000).

[18] R. S. Calsaverini, E. Bernardes, J. C. Egues, and D. Loss, Intersubband-induced spin-orbit interaction in quantum wells, Phys. Rev. B **78**, 155313 (2008).

[19] J. Y. Fu, P. H. Penteado, D. R. Candido, G. J. Ferreira, D. P. Pires, E. Bernardes, and J. C. Egues, Spin-orbit coupling in wurtzite heterostructures, Phys. Rev. B **101**, 134416 (2020).

[20] M. Kammermeier, A. Seith, P. Wenk, and J. Schliemann, Persistent spin textures and currents in wurtzite nanowire-based quantum structures, Phys. Rev. B **101**, 195418 (2020).

[21] D. K. Ross, Alternative models of the real number line in physics, Int. J. Theor. Phys. **23**, 1207 (1984).

[22] G. Dresselhaus, Spin-orbit coupling effects in zinc blende structures, Phys. Rev. **100**, 580 (1955).

[23] G. Engels, J. Lange, T. Schäpers, and H. Lüth, Experimental and theoretical approach to spin splitting in modulation-doped $In_xGa_{(1-x)}As/InP$ quantum wells for $B \to 0$, Phys. Rev. B **55**, R1958 (1997).

[24] J. D. Koralek, C. P. Weber, J. Orenstein, B. A. Bernevig, S.-C. Zhang, S. Mack, and D. D. Awschalom, Emergence of the persistent spin helix in semiconductor quantum wells, Nature (London) **458**, 610 (2009).

[25] M. P. Walser, U. Siegenthaler, V. Lechner, D. Schuh, S. D. Ganichev, W. Wegscheider, and G. Salis, Dependence of the Dresselhaus spin-orbit interaction on the quantum well width, Phys. Rev. B **86**, 195309 (2012).

[26] N. S. Averkiev, L. E. Golub, and M. Willander, Spin relaxation anisotropy in two-dimensional semiconductor systems, J. Phys.: Condens. Matter **14**, R271 (2002).

[27] N. S. Averkiev and L. E. Golub, Giant spin relaxation anisotropy in zinc-blende heterostructures, Phys. Rev. B **60**, 15582 (1999).

[28] D. Iizasa, A. Aoki, T. Saito, J. Nitta, G. Salis, and M. Kohda, Control of spin relaxation anisotropy by spin-orbit-coupled diffusive spin motion, Phys. Rev. B **103**, 024427 (2021).

[29] B. A. Bernevig, J. Orenstein, and S.-C. Zhang, Exact SU(2) Symmetry and Persistent Spin Helix in a Spin-Orbit Coupled System, Phys. Rev. Lett. **97**, 236601 (2006).

[30] M. P. Walser, C. Reichl, W. Wegscheider, and G. Salis, Direct mapping of the formation of a persistent spin helix, Nat. Phys. **8**, 757 (2012).

[31] J. Schliemann, J. C. Egues, and D. Loss, Nonballistic Spin-Field-Effect Transistor, Phys. Rev. Lett. **90**, 146801 (2003).

[32] A. Sasaki, S. Nonaka, Y. Kunihashi, M. Kohda, T. Bauernfeind, T. Dollinger, K. Richter, and J. Nitta, Direct determination of spin-orbit interaction coefficients and realization of the persistent spin helix symmetry, Nat. Nanotechnol. **9**, 1748 (2014).

[33] J. Y. Fu and J. C. Egues, Spin-orbit interaction in GaAs wells: From one to two subbands, Phys. Rev. B **91**, 075408 (2015).

[34] W. Wang, X. M. Li, and J. Y. Fu, Two distinct regimes for the electrical control of the spin-orbit interaction in GaAs wells, J. Magn. Magn. Mater. **411**, 84 (2016).

[35] C.-M. Hu, J. Nitta, T. Akazaki, H. Takayanagai, J. Osaka, P. Pfeffer, and W. Zawadzki, Zero-field spin splitting in an inverted $In_{0.53}Ga_{0.47}As/In_{0.52}Al_{0.48}As$ heterostructure: Band nonparabolicity influence and the subband dependence, Phys. Rev. B **60**, 7736 (1999).

[36] C.-M. Hu, J. Nitta, T. Akazaki, H. Takayanagi, J. Osaka, P. Pfeffer, and W. Zawadzki, Observation of the zero-field spin splitting of the second subband in an inverted $In_{0.53}Ga_{0.47}As/In_{0.52}Al_{0.48}As$ heterostructure, Physica E **6**, 767 (2000).

[37] H. Bentmann, S. Abdelouahed, M. Mulazzi, J. Henk, and F. Reinert, Direct Observation of Interband Spin-Orbit Coupling

in a Two-Dimensional Electron System, Phys. Rev. Lett. **108**, 196801 (2012).

[38] F. G. G. Hernandez, L. M. Nunes, G. M. Gusev, and A. K. Bakarov, Observation of the intrinsic spin Hall effect in a two-dimensional electron gas, Phys. Rev. B **88**, 161305(R) (2013).

[39] E. A. de Andrada e Silva, G. C. La Rocca, and F. Bassani, Spin-orbit splitting of electronic states in semiconductor asymmetric quantum wells, Phys. Rev. B **55**, 16293 (1997).

[40] R. Noguchi, K. Kuroda, K. Yaji, K. Kobayashi, M. Sakano, A. Harasawa, T. Kondo, F. Komori, and S. Shin, Direct mapping of spin and orbital entangled wave functions under interband spin-orbit coupling of giant Rashba spin-split surface states, Phys. Rev. B **95**, 041111(R) (2017).

[41] G. J. Ferreira, F. G. G. Hernandez, P. Altmann, and G. Salis, Spin drift and diffusion in one-and two-subband helical systems, Phys. Rev. B **95**, 125119 (2017).

[42] I. R. de Assis, R. Raimondi, and G. J. Ferreira, Spin drift-diffusion for two-subband quantum wells, Phys. Rev. B **103**, 165304 (2021).

[43] F. G. G. Hernandez, G. J. Ferreira, M. Luengo-Kovac, V. Sih, N. M. Kawahala, G. M. Gusev, and A. K. Bakarov, Electrical control of spin relaxation anisotropy during drift transport in a two-dimensional electron gas, Phys. Rev. B **102**, 125305 (2020).

[44] L. Derkacz and L. Jakóbczyk, Quantum interference and evolution of entanglement in a system of three-level atoms, Phys. Rev. A **74**, 032313 (2006).

[45] H. Sun, S. Q. Gong, Y. P. Niu, S. Q. Jin, R. X. Li, and Z. Z. Xu, Enhancing Kerr nonlinearity in an asymmetric double quantum well via Fano interference, Phys. Rev. B **74**, 155314 (2006).

[46] A. Joshi and M. Xiao, Optical Multistability in Three-Level Atoms inside an Optical Ring Cavity, Phys. Rev. Lett. **91**, 143904 (2003).

[47] S. Ullah, G. M. Gusev, A. K. Bakarov, and F. G. G. Hernandez, Large anisotropic spin relaxation time of exciton bound to donor states in triple quantum wells, J. Appl. Phys. **121**, 205703 (2017).

[48] F. G. G. Hernandez, S. Ullah, G. J. Ferreira, N. M. Kawahala, G. M. Gusev, and A. K. Bakarov, Macroscopic transverse drift of long current-induced spin coherence in two-dimensional electron gases, Phys. Rev. B **94**, 045305 (2016).

[49] S. Ullah, G. M. Gusev, A. K. Bakarov, and F. G. G. Hernandez, Tailoring multilayer quantum wells for spin devices, Pramana J. Phys. **91**, 34 (2018).

[50] S. Wiedmann, N. C. Mamani, G. M. Gusev, O. E. Raichev, A. K. Bakarov, and J. C. Portal, Magnetoresistance oscillations in multilayer systems: Triple quantum wells, Phys. Rev. B **80**, 245306 (2009).

[51] L. Fernandes dos Santos, B. G. Barbosa, G. M. Gusev, J. Ludwig, D. Smirnov, A. K. Bakarov, and Y. A. Pusep, Spectroscopic evidence of quantum Hall interlayer tunneling gap collapse caused by tilted magnetic field in a GaAs/AlGaAs triple quantum well, Phys. Rev. B **89**, 195113 (2014).

[52] H. Cruz and D. Luis, Possibility of spin device in a triple quantum well system, J. Appl. Phys. **104**, 083715 (2008).

[53] T. Iijima and H. Akera, Gate-Voltage-Induced Switching of the Spin-Relaxation Rate in a Triple-Quantum-Well Structure, Phys. Rev. Appl. **13**, 064075 (2020).

[54] T. Koga, J. Nitta, T. Akazaki, and H. Takayanagi, Rashba Spin-Orbit Coupling Probed by the Weak Antilocalization Analysis in InAlAs/InGaAs/InAlAs Quantum Wells as a Function of Quantum Well Asymmetry, Phys. Rev. Lett. **89**, 046801 (2002).

[55] T. Koga, Y. Sekine, and J. Nitta, Experimental realization of a ballistic spin interferometer based on the Rashba effect using a nanolithographically defined square loop array, Phys. Rev. B **74**, 041302(R) (2006).

[56] M. M. Glazov, E. Y. Sherman, and V. K. Dugaev, Two-dimensional electron gas with spin-orbit coupling disorder, Physica E **42**, 2157 (2010).

[57] M. M. Glazov and E. Y. Sherman, Nonexponential spin relaxation in magnetic fields in quantum wells with random spin-orbit coupling, Phys. Rev. B **71**, 241312(R) (2005).

[58] E. Y. Sherman, Random spin-orbit coupling and spin relaxation in symmetric quantum wells, Appl. Phys. Lett. **82**, 209 (2003).

[59] R. Winkler, *Spin-Orbit Coupling Effects in Two-Dimensional Electron and Hole Systems* (Springer, New York, 2003).

[60] I. Vurgaftman, J. R. Meyer, and L. R. Ram-Mohan, Band parameters for III-V compound semiconductors and their alloys, J. Appl. Phys. **89**, 5815 (2001).

[61] M. Lee, M. O. Hachiya, E. Bernardes, J. C. Egues, and D. Loss, Spin Hall effect due to intersubband-induced spin-orbit interaction in symmetric quantum wells, Phys. Rev. B **80**, 155314 (2009).

[62] S. Souma, A. Sawada, H. Chen, Y. Sekine, M. Eto, and T. Koga, Spin Blocker Using the Interband Rashba Effect in Symmetric Double Quantum Wells, Phys. Rev. Appl. **4**, 034010 (2015).

[63] E. Bernardes, J. Schliemann, M. Lee, J. C. Egues, and D. Loss, Spin-Orbit Interaction in Symmetric Wells with Two Subbands, Phys. Rev. Lett. **99**, 076603 (2007).

[64] P. Wójcik and J. Adamowski, Effect of inter- and intra-subband spin-orbit interactions on the operation of a spin transistor with a double quantum well structure, Semicond. Sci. Technol. **31**, 115012 (2016).

[65] Here we mainly consider crossings between neighboring subbands.

[66] J. R. Bindel, M. Pezzotta, J. Ulrich, M. Liebmann, E. Y. Sherman, and M. Morgenstern, Probing variations of the Rashba spin-orbit coupling at the nanometre scale, Nat. Phys. **12**, 920 (2016).

[67] J. Nitta, Ready for a close-up, Nat. Phys. **12**, 898 (2016).

[68] C. X. Liu, T. L. Hughes, X. L. Qi, K. Wang, and S. C. Zhang, Quantum Spin Hall Effect in Inverted Type-II Semiconductors, Phys. Rev. Lett. **100**, 236601 (2008).

[69] A. J. A. Beukman, F. K. de Vries, J. van Veen, R. Skolasinski, M. Wimmer, F. Qu, D. T. de Vries, B. M. Nguyen, W. Yi, A. A. Kiselev, M. Sokolich, M. J. Manfra, F. Nichele, C. M. Marcus, and L. P. Kouwenhoven, Spin-orbit interaction in a dual gated InAs/GaSb quantum well, Phys. Rev. B **96**, 241401(R) (2017).